JOURNAL OF COMPUTATIONAL PHYSICS 60, 76–96 (1985)

The Calculation of Stellarator Equilibria in Vacuum Flux Surface Coordinates*

T. C. HENDER, B. A. CARRERAS, L. GARCIA, AND J. A. ROME

Fusion Energy Division, Oak Ridge National Laboratory, Oak Ridge, Tennessee 37831

AND

V. E. LYNCH

Computer Sciences, Oak Ridge National Laboratory, Oak Ridge, Tennessee 37831

Received June 12, 1984; revised September 10, 1984

Details are given of a three-dimensional stellarator equilibrium code NEAR. This code uses a set of vacuum flux coordinates as a Eulerian grid for the equilibrium calculations. This coordinate system provides an economic representation of the complex geometry associated with stellarators. The equilibrium equations are solved by an energy minimization technique employing a conjugate gradient iteration scheme. The results of extensive numerical convergence studies are presented. Also comparisons with existing codes are made to benchmark the NEAR code.

1. INTRODUCTION

The study of magnetohydrodynamic (MHD) equilibria in stellarator configurations is greatly complicated by the fully three-dimensional (3-D) nature of the device. Several approximations may be introduced that permit analytic or semi-analytic equilibrium solutions. The method of averaging, in which the vacuum helical magnetic field is treated as a rapidly fluctuating small scale perturbation to the dominant toroidal field reduces the stellarator equilibrium problem to a two-dimensional (2-D) problem [1]. An alternate analytic approach has been to make an expansion about the magnetic axis [2].

To study stellarator equilibria without asymptotic expansions generally requires the use of numerical methods. Most of the numerical approaches use a variational technique to solve for the equilibria. The Chodura–Schlüter code [3] solves the equilibrium equations by minimizing the energy on a cylindrical coordinate Eulerian grid. The Bauer, Betancourt, and Garabedian code [4] solves the so-

0021-9991/85 $3.00

called inverse equilibrium problem, in which the equilibrium problem is reformulated into that of solving for the flux coordinates, instead of solving directly for magnetic fields and pressure.

In this paper, the NEAR code, which solves the 3-D equilibrium problem directly by an energy minimization technique, will be described. The NEAR code formulation is similar to that of the Chodura–Schlüter code except that a vacuum flux coordinate system is employed as the Eulerian frame of reference for the calculation. An Eulerian formulation is chosen because it allows the study of equilibria whose flux surface topology changes with pressure. The vacuum flux coordinates (ρ, θ, ϕ) are obtained numerically from the vacuum magnetic fields specified by a given coil configuration. The metric elements and Jacobian of the flux coordinates are represented by Fourier series in the generalized poloidal (θ) and toroidal (ϕ) angles of the flux coordinates. Details of the vacuum flux coordinates will be given in Section 2. The dependent variables in the equilibrium computation are also represented as Fourier series in θ, ϕ. In the radial direction (ρ), a finite difference representation is used. Using the vacuum flux coordinates in this manner, as an Eulerian grid, will be shown to provide a far more efficient description of geometrically complicated stellarator equilibria than the spatial coordinate finite difference representation used in Chodura–Schlüter code. This permits a much finer spatial numerical resolution to be achieved. The equilibrium equations and their solution by the NEAR code algorithm will be described in Section 3. To illustrate the numerical properties of NEAR, equilibrium results will be shown in Section 4, for the Advanced Toroidal Facility (ATF) configuration [5], and for a 12-field-period heliac [6]. For the ATF equilibria, comparisons will be made with other computations. Finally, in Section 5, conclusions will be given.

2. Vacuum Flux Coordinates

The flux coordinate system employed is that described by Boozer [7]. For a vacuum, the magnetic field may be described in contravariant form as

$$\mathbf{B}_v = B_0 \rho \nabla \rho \times \nabla(\theta - \iota\phi) \tag{1}$$

or in covariant form as

$$\mathbf{B}_v = F_v \nabla \phi \tag{2}$$

where $\iota(\rho)$ is the rotational transform, F_v is a constant, and $B_0\rho^2/2 = \psi_T$ is the toroidal flux. The role of a radial variable is taken by ρ. The potential ϕ may be regarded as a toroidal variable and for appropriate choice of the constant F_v, ϕ changes by 2π in traversing the torus once toroidally. Finally, the role of a poloidal angle is taken by θ, which changes by 2π in going once around the torus poloidally.

These coordinates are generated numerically in a manner described by Kuo-Petravic *et al.*, using the method and code described in Ref. [8]. This code

generates the Fourier series representation of the cylindrical coordinates (R, Z, ζ) in the vacuum flux coordinates θ and ϕ, by following vacuum magnetic field lines. In most stellarators there is a toroidally repetitive structure to the coils and the machine is composed of a series of identical field periods or modules. Also, within each field period a symmetry exists; at equal toroidal angle distances from either end of the field period, the R coordinates of the coils will be the same, while the Z coordinates will be equal and opposite. This symmetry means that for an appropriate choice of flux coordinate origin, the Fourier representation of R contains only cosine terms and those of Z and $(\zeta - \phi)$, only sine terms. Thus, for example,

$$R(\rho, \theta, \phi) = \sum_{m,n} R_{m,n}(\rho) \cos(m\theta + n\phi), \tag{3}$$

where n is restricted to multiples of the number of field periods (including $n = 0$). In practice, of course, only a finite number of terms may be retained in these Fourier series descriptions. Figure 1 shows how error in representing the vacuum quantities R, Z, and $|\mathbf{B}|$ depends on the number of terms in the Fourier series. Here the error is defined as

$$\underset{-\pi < \theta, \phi < \pi}{\text{Max}} \left(\frac{|\sum_{m,n} A_{m,n} \cos(m\theta + n\phi) - A(\theta, \phi)|}{|A(\theta, \phi)|} \right);$$

that is, the maximum difference between the true value and the value from the Fourier series with a given number of terms, normalized to the true value. The particular case illustrated in Fig. 1 is for the planar axis ATF device. The order in which the $A_{m,n}$ are included in the Fourier series is chosen to optimize its convergence. At 7 harmonics the modes retained are $(m = 0 \to 2,\ n = 0)$ and $(m = -3 \to 0,\ n = 12)$, and at 17 harmonics the modes are $(m = 0 \to 4,\ n = 0)$, $(m = -5 \to 2,\ n = 12)$ and $(m = -3 \to -1,\ n = 24)$. It can be seen that the Fourier representation provides an economic and rapidly convergent description of the vacuum fields. Typically between 10 and 20 harmonics are used to describe the

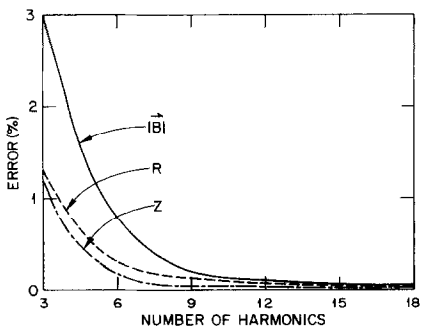

FIG. 1. Error in representing R, Z, and $|\mathbf{B}|$ as Fourier series with a given number of terms.

vacuum quantities in the equilibrium calculation. Helical axis configurations, however, generally have a broader Fourier spectra and may require more harmonics to adequately represent the vacuum fields.

Using the Fourier representations of R, Z, and ζ, the metric elements may be computed. Using (ρ, θ, ϕ) as the independent spatial coordinates leads to singularities in some of the dependent variables and metric elements, at $\rho = 0$. Such singularities are numerically undesirable and may be avoided by rescaling some of the variables by appropriate powers of ρ. The necessary rescalings are $\hat{A}^\theta = \rho A^\theta$, $\hat{A}_\theta = A_\theta/\rho$, $\hat{g}_{\theta\theta} = g_{\theta\theta}/\rho^2$, $\hat{g}_{\rho\theta} = g_{\rho\theta}/\rho$, $\hat{g}^{\theta\theta} = \rho^2 g^{\theta\theta}$, and $\hat{g}^{\rho\theta} = \rho g^{\rho\theta}$. Rescaling in this manner leads to a system of coordinates and vector operators which are very similar to ordinary cylindrical coordinates. For the remainder of this paper, these rescalings will be assumed. Thus, for example, the inverse Jacobian is

$$G_v = \nabla\rho \times \nabla\theta \cdot \nabla\phi = \frac{|\mathbf{B}_v|^2}{B_0 F_v \rho} \tag{4}$$

and

$$g_{\theta\theta} = \frac{1}{\rho^2}\left[\left(\frac{\partial R}{\partial \theta}\right)^2 + R^2\left(\frac{\partial \zeta}{\partial \theta}\right)^2 + \left(\frac{\partial Z}{\partial \theta}\right)^2\right]. \tag{5}$$

Various interrelationships show that the only independent metric elements which must be computed are $g_{\rho\rho}$, $g_{\rho\theta}$, and $g_{\theta\theta}$.

Having solved the equilibrium problem in these flux coordinates, it is desirable to be able to view the solutions in real space. This may easily be achieved using the R, Z, and ζ transformations [e.g., Eq. (3)]. In particular, the magnetic surfaces are computed by following magnetic field lines in the vacuum flux coordinates and recording the points at which they puncture given constant toroidal angle (ζ) planes. The coordinates of these punctures are then transformed to real space coordinates and the magnetic surfaces are plotted. This procedure is more accurate than transforming to real space and then following magnetic field lines; particularly (since as explained in the next section) $\nabla \cdot \mathbf{B} = 0$ is maintained to the accuracy of the finite difference approximations throughout the equilibrium calculation in the vacuum flux coordinates.

3. Equilibrium Equations and Numerics

(a) *Equilibrium Equations*

The approach to solving the equilibrium problem is the same as that of the Chodura–Schlüter code [3]. As a means of reducing the energy, a fictitious force $\mathbf{F}$ is introduced

$$\mathbf{F} = (\nabla \times \mathbf{B}) \times \mathbf{B} - \nabla P. \tag{6}$$

This force is related to a velocity using a conjugate gradient iteration scheme

$$\mathbf{V}^{n+1} = \mathbf{F}^{n+1} + \alpha \frac{\langle \mathbf{F}^2 \rangle^{n+1}}{\langle \mathbf{F}^2 \rangle^n} \mathbf{V}^n, \tag{7}$$

where superscripts denote iteration level, angled brackets denote a volume average, and α is a constant. For optimal convergence α is chosen just less than unity [3]. Using this velocity, the magnetic field $\mathbf{B}$, is advanced in a flux conserving manner,

$$\frac{\partial \mathbf{B}}{\partial t} = \nabla \times (\mathbf{V} \times \mathbf{B}). \tag{8}$$

The pressure P, which is related to the density by the adiabatic pressure law, is advanced in a mass conserving manner,

$$\frac{\partial P}{\partial t} = -\mathbf{V} \cdot \nabla P - \gamma P \nabla \cdot \mathbf{V}, \tag{9}$$

where γ is the ratio of specific heats. It should be noted that instead of the constraint of flux conservation, an alternate constraint of zero net toroidal current is often applied in stellarator equilibrium calculations [4, 10]. A version of the NEAR code which uses this alternate constraint is under development and will be the subject of a future publication. From Eqs. (6), (8), and (9), the rate of change of potential energy is

$$\frac{dW}{dt} \equiv \frac{d}{dt} \int (P/(\gamma - 1) + B^2/2)\, d\tau = -\int \mathbf{V} \cdot \mathbf{F}\, d\tau. \tag{10}$$

Thus, if $\mathbf{V} \cdot \mathbf{F}$ is positive definite, the potential energy will always decrease and the final steady state will be an equilibrium [$\nabla P = \mathbf{J} \times \mathbf{B}$]. In Ref. [3], several iteration schemes for relating $\mathbf{V}$ and $\mathbf{F}$ are investigated. It is shown that the conjugate gradient method [Eq. (7)] is one of the more optimal convergence schemes. Of the other iteration schemes investigated in Ref. [3], the simplest is the friction model $\mathbf{V} = \alpha \mathbf{F}$; however, it is shown that this method has a very slow convergence rate. This convergence rate is greatly improved by a technique employing Chebychev Polynomials which permit large timesteps to be taken. An alternate improvement to the friction model is the gradient method in which the displacement, in the direction of the force, necessary to cause a local energy minimum, is estimated and used. The final method investigated in Ref. [3] is the conjugate gradient method which improves on the gradient method by incorporating information from the previous iteration step. The conjugate gradient method is simpler to implement than the Chebychev method and is used without further investigation in the work described in this paper.

(b) *Numerical Algorithm and Differencing*

In the numerical implementation of the above equations [Eqs. (6) through (9)] the dependent variables are V^ρ, V^θ, V^ϕ, (B^θ/D_v), (B^ϕ/D_v), and P [where $D_v = \rho G_v$]. The main reason for time advancing $(\mathbf{B}/D_v)$ instead of $\mathbf{B}$ is that in the flux coordinates $\nabla \cdot \mathbf{B} = 0$, is

$$\frac{1}{\rho}\frac{\partial}{\partial \rho}\left(\rho \frac{B^\rho}{D_v}\right) + \frac{1}{\rho}\frac{\partial}{\partial \theta}\left(\frac{B^\theta}{D_v}\right) + \frac{\partial}{\partial \phi}\left(\frac{B^\phi}{D_v}\right) = 0. \tag{11}$$

Thus (B^ρ/D_v) may be computed from Eq. (11), once (B^θ/D_v) and (B^ϕ/D_v) have been time advanced. This procedure maintains the important physical property that $\nabla \cdot \mathbf{B} = 0$, throughout the calculation, and is also more efficient than time advancing (B^ρ/D_v) directly.

The numerical algorithm used in the NEAR code is summarized in the flow diagram shown in Fig. 2. The dependent variables are represented in finite difference form in the radial direction (ρ). The variables V^ρ and (B^ρ/D_v) are discretized on a uniformly spaced ρ-mesh, whose first point is the coordinate axis $(\rho = 0)$ and whose last point is at the wall. The remaining variables $[V^\theta, V^\phi, (B^\theta/D_v), (B^\phi/D_v)$, and $P]$ are on an intermediate mesh whose points lie halfway between those of the V^ρ, (B^ρ/D_v) mesh. Centered finite differences are used to approximate the ρ derivatives. In an earlier version of the NEAR code, all the dependent variables were represented on the same radial mesh. This however, led to

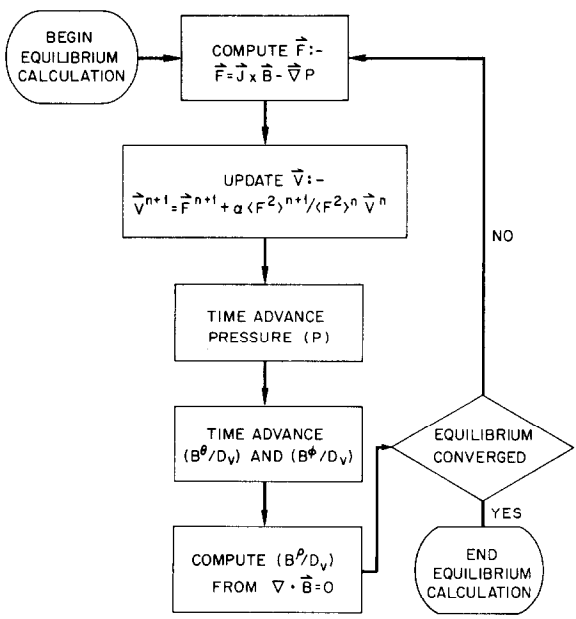

FIG. 2. Flow diagram of the NEAR algorithm.

grid separation problems arising from the hyperbolic nature of the equations—the highest derivatives that are present are first order, which only effectively couple every other grid point and thus permit grid separation. By using the two distinct grids as previously described, these grid separation problems are overcome.

Since the metric elements are represented as Fourier series in θ and ϕ it is natural to also represent the dependent variables in this manner. The symmetry arising from the coils which was discussed in Section 2 means that (B^ρ/D_v), V^θ, V^ϕ can be represented by sine series and (B^θ/D_v), (B^ϕ/D_v), V^ρ, and P can be represented by cosine series. Thus, for example,

$$V^\rho(\rho, \theta, \phi, t) = \sum_{m,n} V^\rho_{m,n}(j, t) \cos(m\theta + n\phi). \tag{12}$$

This Fourier representation requires that the convolutions of Fourier series be calculated numerically. These convolutions are performed numerically using the simple trigonometric formulae for the products of sines and cosines. Fast Fourier transforms are not used to compute these convolutions. The choice of the (m, n) spectrum used in the calculations will be discussed in the next section. Simple first order explicit differencing is used in time. The finite difference form of the equations solved is given in the Appendix.

(c) *Boundary and Initial Conditions*

The magnetic field is initialized to its numerically obtained vacuum value:

$$\begin{aligned} \frac{B^\rho}{D_v} &= 0, \\ \frac{B^\theta}{D_v} &= B_0 \iota \rho, \\ \frac{B^\phi}{D_v} &= B_0. \end{aligned} \tag{13}$$

The velocity is initialized to zero, and the initial pressure (P_I) is assumed to be of the form

$$P_I = a(1 - \rho^2)^m, \tag{14}$$

where a and m are constants (for all the results presented in this paper, $m = 2$). In the code, analytic forms are used for the radial derivatives of the initial pressure (P_I) occurring in Eqs. (6) and (9).

The boundary conditions are those of an infinitely conducting wall at the last closed vacuum flux surface. The boundary conditions on the radial velocity and magnetic field are

$$V^\rho|_{\text{wall}} = \left(\frac{B^\rho}{D_v}\right)\Bigg|_{\text{wall}} = 0. \tag{15}$$

The remaining dependent variables are on the intermediate mesh and their values are never required at the wall. At the coordinate axis ($\rho = 0$) regularity imposes certain constraints on the behavior of the dependent variables. In particular, the (m, n) component of V^ρ, V^θ, (B^ρ/D_v), (B^θ/D_v) must go to zero at least as fast as $\rho^{||m|-1|}$ and V^ϕ, (B^ϕ/D_v), P must go to zero at least as fast as $\rho^{|m|}$. The additional constraints that

$$V^\rho_{m,n} = -mV^\theta_{m,n} \tag{16}$$

and

$$\left(\frac{B^\rho}{D_v}\right)_{m,n} = m\left(\frac{B^\theta}{D_v}\right)_{m,n}$$

must also be satisfied by the $m = 1$ components at $\rho = 0$. For the dependent variables (B^θ/D_v), (B^ϕ/D_v), V^ϕ, P an additional mesh point is included at $\rho = 0$. The variables V^ρ, V^ϕ, (B^θ/D_v), (B^ϕ/D_v), and P are advanced in time at the origin, using one-sided approximations to the radial derivatives, and values of the $m = 1$ components of V^θ and (B^ρ/D_v) are determined using Eqs. (16).

4. Computational Results

In this section, the numerical properties of the NEAR code will be investigated by studying equilibria for the planar axis ATF and for a 12-field-period heliac. For each new configuration studied the convergence properties must be examined. The results given here for the heliac and ATF are fairly representative of machines of their class. The ATF device, in its standard mode of operation, is a 12-field period $l = 2$ torsatron with a rotational transform (ι) varying between ~ 0.3 at the magnetic axis and ~ 1.0 at the plasma edge.

There are several parameters for which numerical convergence studies must be made. First the selection of (m, n) mode pairs to be included in the equilibrium calculations will be considered. As a general rule, the importance of a mode in the vacuum representation gives a good guide to the importance of that mode in the equilibrium calculation. This is because a large harmonic in the metric elements and Jacobian leads to good couplings to that particular harmonic during the evolution to an equilibrium. Figure 3 shows the dominant harmonics of $|B|^2$ as function of ρ for the ATF vacuum. The $(1, 0)$ harmonic is associated with the toroidicity, while the $(-2, 12)$ harmonic is due to the helical coils. The $(-1, 12)$ and $(-3, 12)$ harmonics are the toroidal side-bands of the $(-2, 12)$ harmonic. Figure 4 shows the spectrum of energies $E_{m,n}$ for the planar axis ATF at $\beta_0 = 5\%$, where

$$E_{m,n} = \int_0^{\text{wall}} \rho \left(\frac{B^2_{m,n}}{2} + \frac{P_{m,n}}{\gamma - 1}\right) d\rho. \tag{17}$$

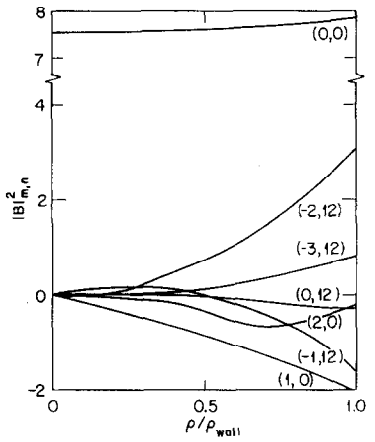

FIG. 3. Dominant $B^2_{m,n}$ in the vacuum representation of the planar axis ATF.

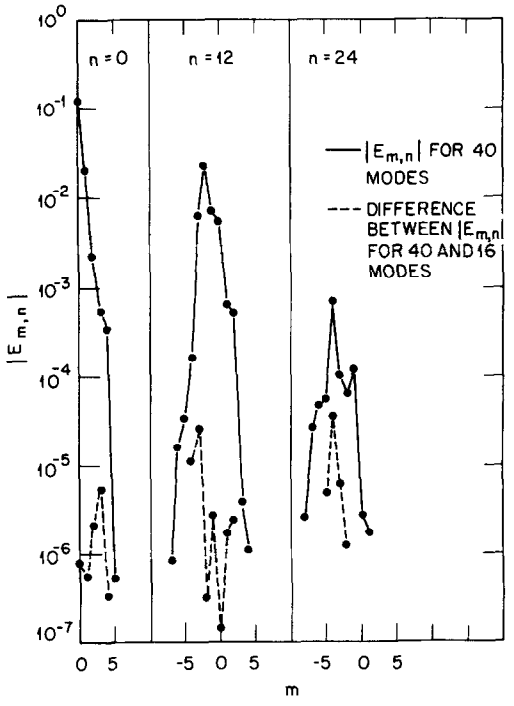

FIG. 4. $E_{m,n}$ spectrum for $\beta_0 = 5\%$ planar axis ATF. Solid curve is for a 40-mode case and the broken curve is the difference between the $E_{m,n}$ for 40 and 16 modes.

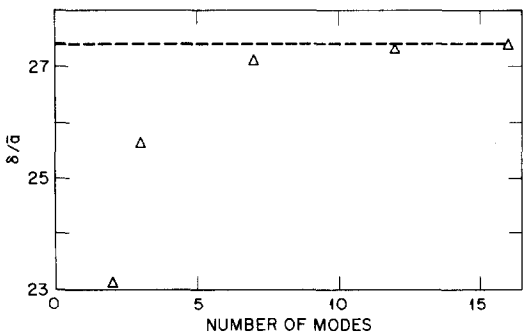

FIG. 5. Convergence of equilibrium shift with number of modes for $\beta_0 = 5\%$ planar axis ATF.

The solid curves in Fig. 4 are the spectrum for a simulation in which 40 modes are retained with 34 radial grid points. The broken curves in Fig. 4 are the differences of the $E_{m,n}$ between a 16- and 40-mode simulation. Good convergence with number of modes is evident with 16 modes. The dominant modes in the finite-β spectrum can be seen to be precisely the dominant vacuum modes (c.f. Fig. 3). A logarithmic fall off in m and n about the dominant $E_{m,n}$ occurs. This relatively rapid falloff means that the gross equilibrium properties such as equilibrium shift converge very rapidly. Figure 5 shows how the equilibrium shift converges as the number of modes retained in the equilibrium calculation increases, for the same case as Fig. 4. A very rapid convergence of the equilibrium shift is evident. The first two modes retained in Fig. 5 are the (0, 0) and (1, 0). The largest mode set represented in Fig. 5 corresponds to the 16-mode set, whose spectrum is shown in Fig. 4. For a flux conserving calculation, the rotational transform (ι) profile as a function of toroidal flux should be a conserved quantity. Figure 6 shows how the ι profile depends on the number of modes retained in the calculation at $\beta_0 = 5\%$. In Fig. 7 the flux surfaces are shown for the $\beta_0 = 5\%$ ATF equilibrium with 2, 7, and 16 modes retained

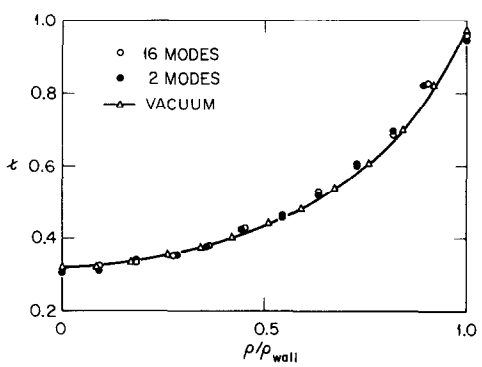

FIG. 6. Dependence of ι profile on number of modes for $\beta_0 = 5\%$ planar axis ATF. (Vacuum ι profile is shown for reference.)

in the calculation. All of these mode convergence results show very rapid convergence. At higher betas the spectrum broadens somewhat, but 20 modes are still sufficient to give converged results at $\beta_0 = 15\%$.

For ATF the equilibrium shift is toroidally dominated, which means that the equilibrium can be well reproduced with only two modes [the (0, 0) and (1, 0)]. For other devices, such as heliacs, the vacuum mode spectrum is much broader, and the toroidal and helical shifts may be comparable. The net result is that heliacs require many more harmonics (typically $\geqslant 25$), for a well converged equilibrium. Figure 8 shows the $E_{m,n}$ spectrum ($\beta_0 = 15\%$) for a 12-field-period heliac which has an ι profile varying between 4.55 at the magnetic axis and 5.33 at the plasma edge, and a coil aspect ratio of 12. Seventy modes and 30 radial grid points were used in the calculation associated with this spectrum. The broader character of this spectrum compared to the planar axis ATF spectrum (Fig. 4) is evident. Figure 9 shows the vacuum and equilibrium flux surfaces for this case. Even though several

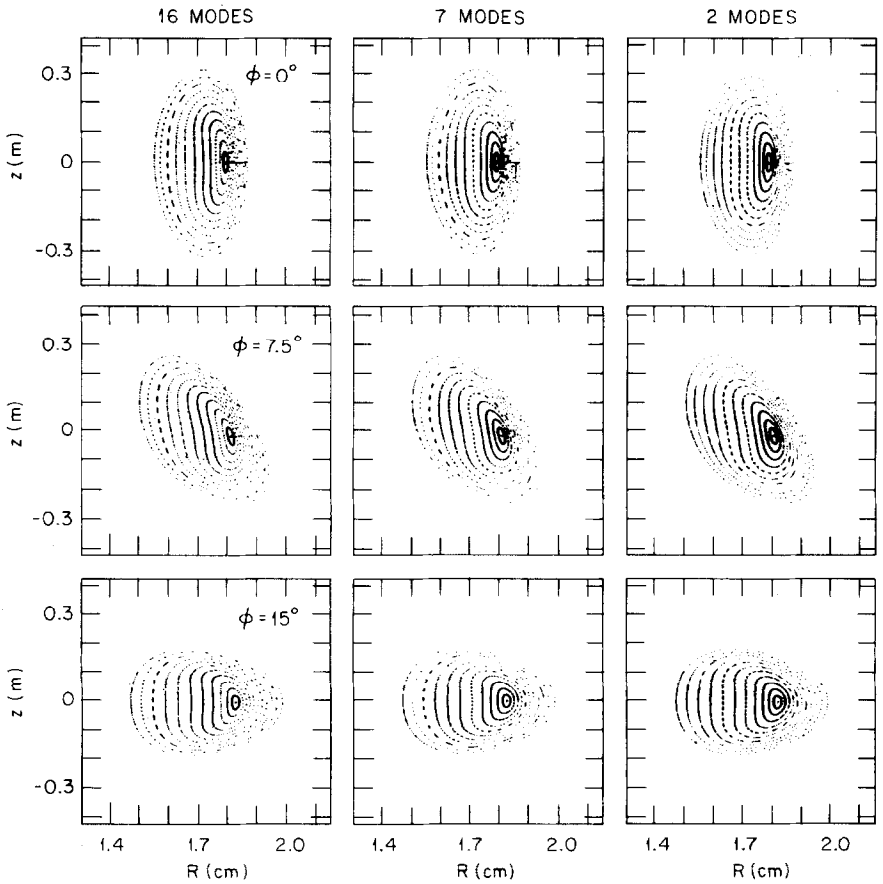

FIG. 7. Convergence of flux surfaces with number of modes for $\beta_0 = 5\%$ planar axis ATF.

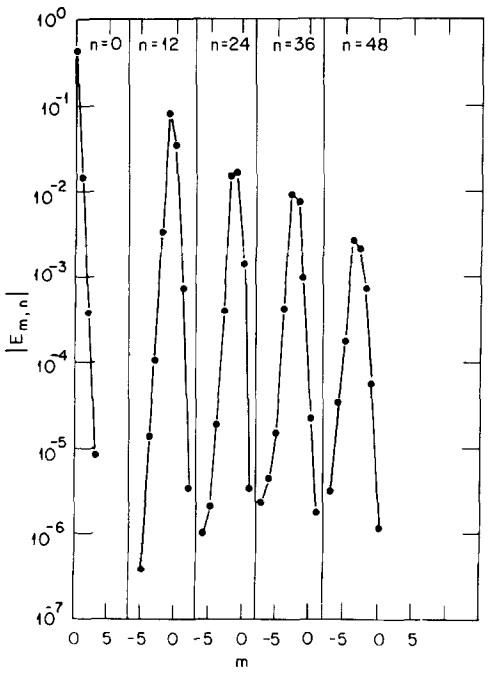

FIG. 8. $E_{m,n}$ spectrum for a 70-mode simulation of a 12-field-period heliac ($\beta_0 = 15\%$).

resonant and nearly resonant harmonics are present in the calculation, no breaking or significant distortions to the flux surfaces are evident.

Another convergence property which must be studied is that of the radial mesh. Figure 10 shows how the ι profile and magnetic well profile converge with increasing radial mesh at 5% central beta for ATF (16 modes). The convergence studies shown in Fig. 10 show surprisingly good results with only seven radial mesh points; these results are, however, consistent with similar convergence studies for the Chodura–Schlüter code [9]. The 25-mesh-point calculation shown in Fig. 10 required about 20 min of CPU time on a Cray-I computer. For rapid parameter scans of devices with toroidally dominated shifts only two modes and about 10 mesh points are required. Such calculations require only a couple of minutes of Cray-I CPU time. Convergence studies of the $E_{m,n}$ spectrum with radial mesh show that 25 radial mesh points are sufficient to resolve the dominant harmonics (those shown in Fig. 3) to an accuracy of 0.1% at $\beta = 5\%$ for the planar axis ATF. Also, 25 mesh points yield an equilibrium shift converged to 0.3% accuracy. Thus, it can be concluded that at $\beta_0 = 5\%$, the planar axis ATF requires between 20 and 30 radial mesh points for converged equilibrium solutions. At higher beta somewhat finer meshes are required—for example, at $\beta_0 = 15\%$ the errors in the $E_{m,n}$ become approximately a factor of 1.5 worse than the equivalent errors for the $\alpha_0 = 5\%$ case. Figure 11 shows how the $\beta_0 = 5\%$ ATF equilibrium flux surfaces converge for increasingly fine meshes.

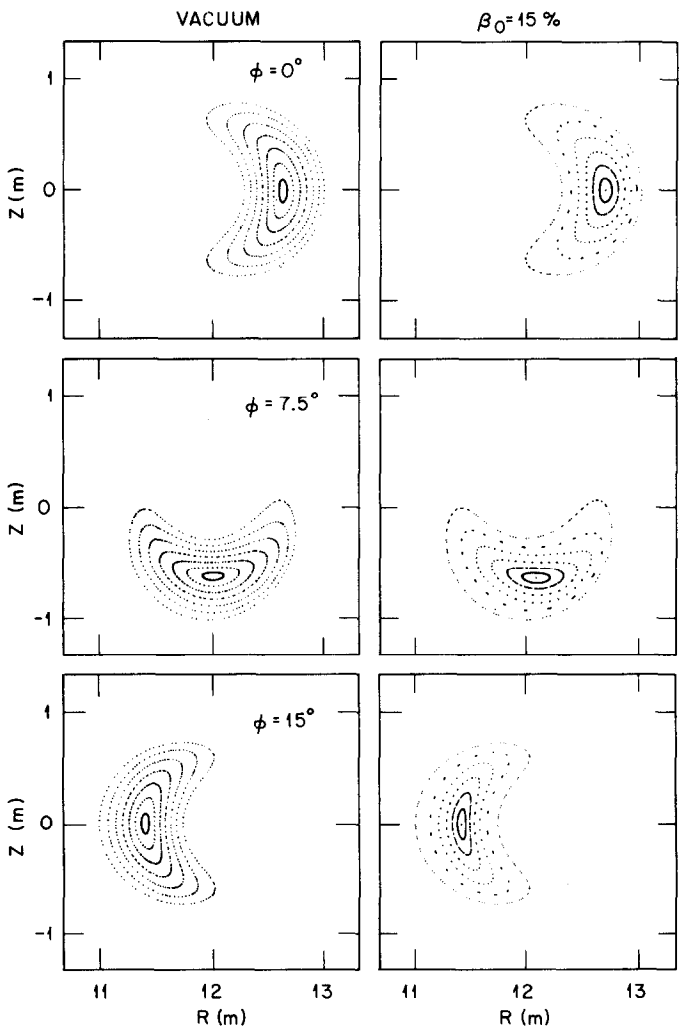

FIG. 9. Flux surfaces for the 12-field-period heliac whose spectrum is shown in Fig. 8.

The convergence of the solutions with the timestep size used in time advancing **B** and P has also been studied. Typically, a timestep two or three times smaller than that permitted by numerical stability considerations is used. The convergence of the solution with timestep size is regularly checked by reducing the timestep and repeating the calculation.

The most important cnvergence is the convergence toward a solution of the equilibrium equations. The equilibrium iteration scheme makes use of a volume average of the force $[\langle \mathbf{F}^2 \rangle]$ which provides a sensitive measure of the equilibrium convergence. Figure 12 shows how $\langle \mathbf{F}^2 \rangle$ decreases as a function of iteration during

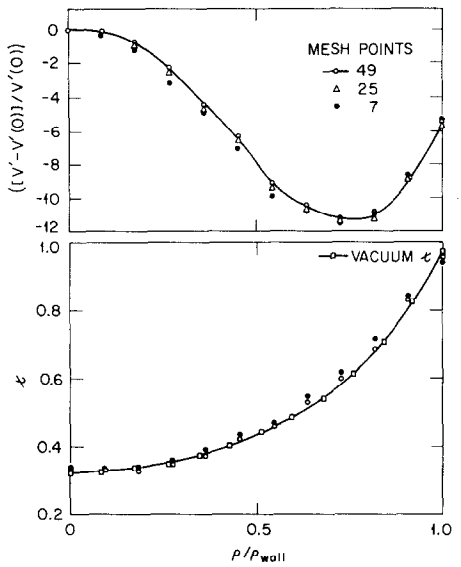

FIG. 10. Dependence of magnetic well (upper plot) and ι profile (lower plot) on number of radial grid points for the $\beta_0 = 5\%$ planar axis ATF.

a $\beta_0 = 5\%$, ATF equilibrium calculation. Also shown in Fig. 12 is the history of equilibrium shift during the calculation. The conjugate gradient iteration scheme gives a rapid logarithmic reduction of $\langle \mathbf{F}^2 \rangle$ and convergence of the shift. No attempt has been made to examine alternate convergence schemes. The fact that the $\langle \mathbf{F}^2 \rangle$ saturates at some final value is due to the numerical resistivity arising from radial differencing errors. The final value of $\langle \mathbf{F}^2 \rangle$ scales approximately as $(\Delta\rho)^{-2}$, where $\Delta\rho$ is the radial mesh size.

Another measure of the equilibrium convergence is given by the requirement that for an exact equilibrium $\mathbf{B} \cdot \nabla P = 0$. To measure how well the NEAR equilibria satisfy this relation the variance of the pressure on a magnetic surface is calculated as a diagnostic. Here the variance is defined as

$$\bar{P} = \frac{[(\int P dl)^2 - \int P^2 dl]^{1/2}}{\int P dl} \tag{18}$$

where the path of the integral is along a magnetic field line and the asymptotic value of $\bar{P}$ is obtained by following the field line for many turns. Figure 13 shows $\bar{P}$ as function of radius for a $\beta_0 = 5\%$, 16-mode, 34-radial-mesh-point equilibrium. The error $(\bar{P})$ is almost entirely due to radial differencing errors arising during the equilibrium calculation and also during the evaluation of $\bar{P}$. This error scales as $(\Delta\rho)^{-2}$ but is relatively insensitive to the number of modes retained in the equilibrium calculation. Although this diagnostic provides a further validation of

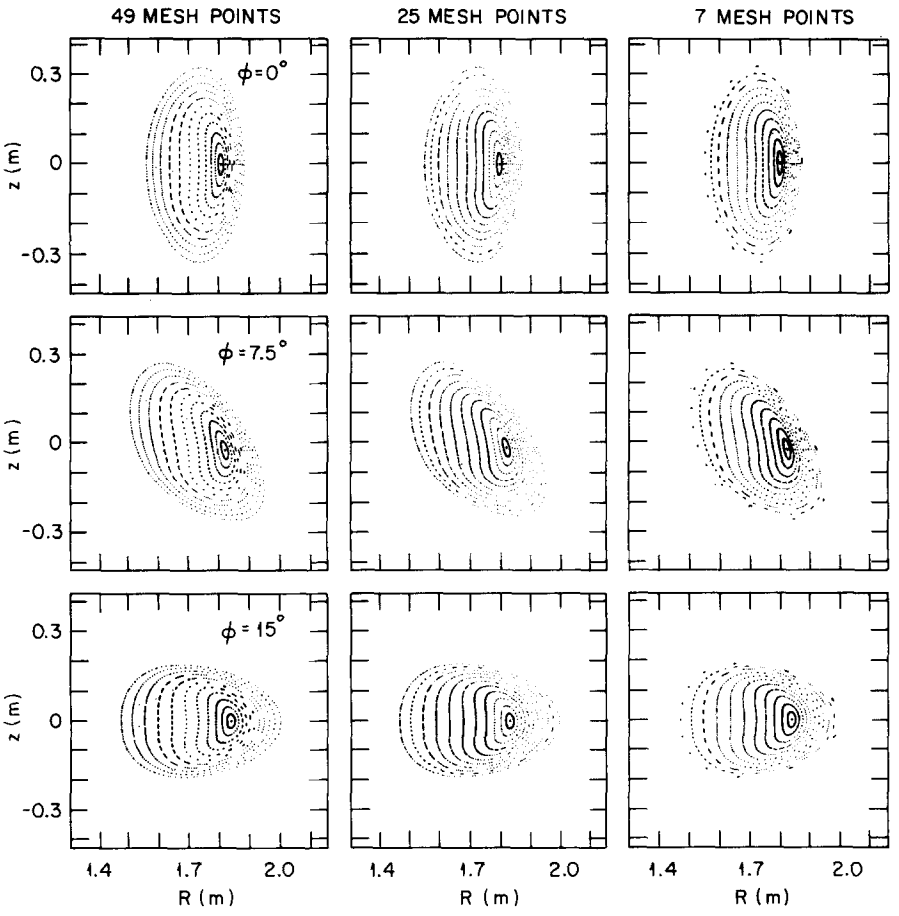

FIG. 11. Convergence of flux surfaces with number of radial grid points for the $\beta_0 = 5\%$ planar axis ATF.

the code, the gross equilibrium properties, such as shift, magnetic well, and ι profile provide much better measures of the necessary resolution for convergence.

The results of calculations with the NEAR code have been benchmarked against various other codes. Some of these comparisons are given in Ref. [10]. Here the NEAR equilibrium calculations for ATF will be compared with results from the Chodura–Schlüter code. Figure 14 shows a comparison of the equilibrium flux surfaces ($\beta_0 = 5\%$) between the two equilibrium codes. To make this comparison more quantitative, the equilibrium shift and magnetic well profile computed with the Chodura–Schlüter code and NEAR are compared in Figs. 15 and 16, respectively. The good agreement between the NEAR code and the other codes provides a valuable validation of the NEAR code. Finally in Fig. 17, the magnetic well depth as a function of β_0, computed with the NEAR code and Chodura–Schlüter code are

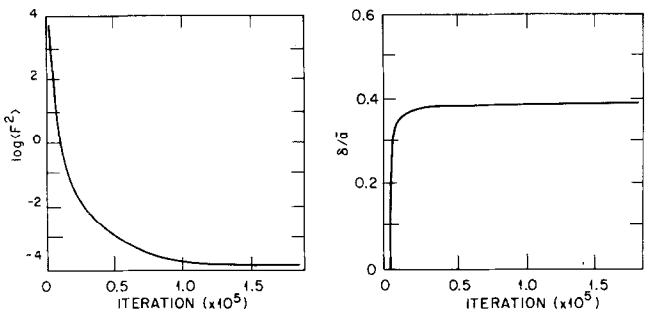

FIG. 12. Residual force $\langle \mathbf{F}^2 \rangle$ and equilibrium shift $(\delta/\bar{a})$ for a $\beta_0 = 5\%$ planar axis ATF calculation.

compared. At low beta ($\lesssim 7\%$) the codes agree well. At higher betas, where the resolution of the Chodura–Schlüter code is less adequate, the agreement deteriorates.

5. CONCLUSIONS

Details of a 3-D stellarator equilibrium code (NEAR) have been given. This code employs the vacuum flux coordinates described by Boozer, as an Eulerian frame of reference. These coordinates have been shown to provide an efficient representation of the complex stellarator geometry. The NEAR code solves the equilibrium equations in these coordinates, subject to the constraints of flux and mass conservation. The code relaxes the equations to an equilibrium by an energy minimization technique. A Fourier series representation is used in the poloidal (θ) and toroidal (ϕ) directions, and a finite difference representation is used in the radial direction (ρ). A first order explicit scheme is used to time-advance the magnetic field and pressure.

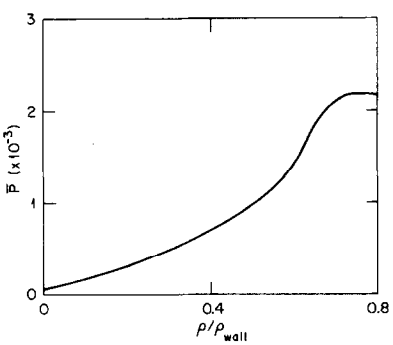

FIG. 13. Variance of the pressure ($\bar{P}$) as a function of radius for planar axis ATF (parameters given in the text).

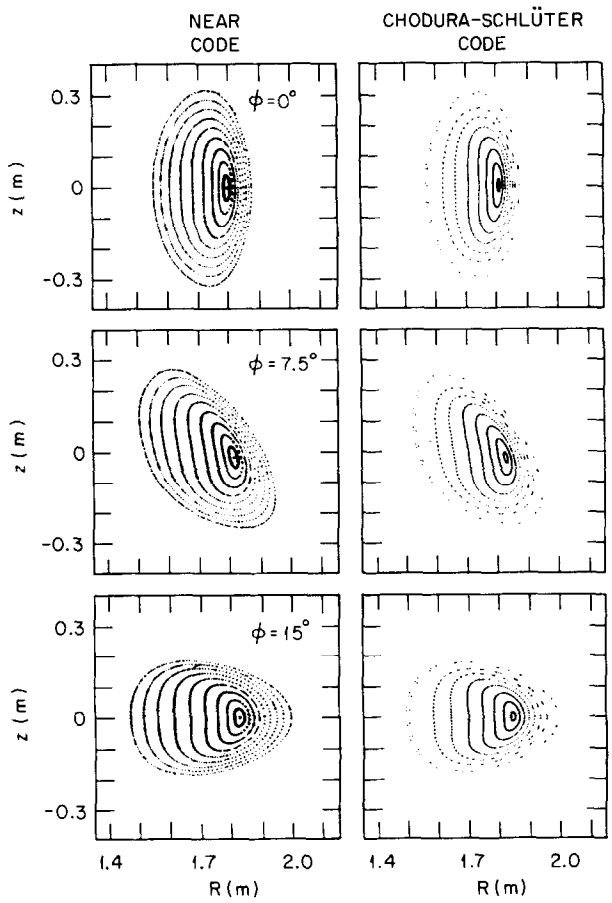

FIG. 14. Comparison of the equilibrium flux surfaces computed with NEAR and Chodura–Schlüter code for the planar axis ATF ($\beta_0 = 5\%$).

Equilibrium convergence studies are presented for the planar axis ATF. The vacuum mode spectrum is shown to provide a good guide of the relative importance of a given mode in the equilibrium calculations. Convergence studies in the number of radial mesh points show that between 20 and 30 points are sufficient. Also the equilibrium properties of a 12-field-periodic heliac have been briefly examined. It is found that heliacs have broader spectra and require more modes for converged results than the planar axis ATF.

The NEAR code has been benchmarked against existing stellarator equilibrium codes. Comparisons of flux surfaces, equilibrium shift, and magnetic well profiles with the Chodura–Schlüter code show good agreement—thus further validating the code.

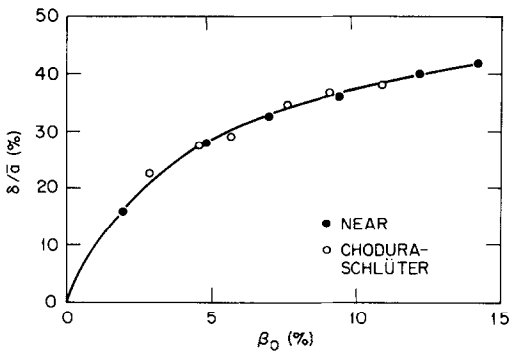

FIG. 15. Comparison of equilibrium shift computed with NEAR and the Chodura–Schlüter code for the planar axis ATF.

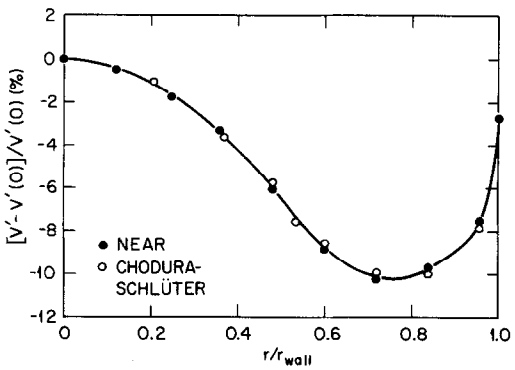

FIG. 16. Comparison of the magnetic well profile computed with NEAR and Chodura–Schlüter code for the equilibrium shown in Fig. 14 ($\beta_0 = 5\%$).

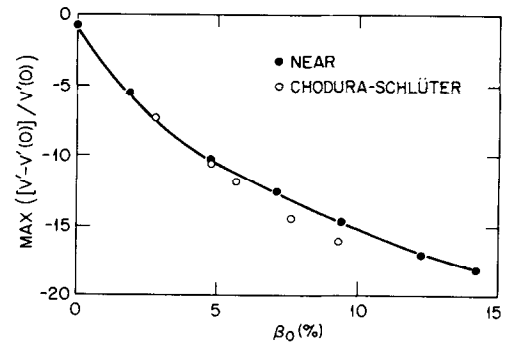

FIG. 17. Comparison of magnetic well depth as a function of β_0 between NEAR and the Chodura–Schlüter code for the planar axis ATF.

APPENDIX: FINITE DIFFERENCE FORM OF THE NEAR EQUATIONS

The following notation will be used in this appendix—a bracket around a variable denotes the (m, n) Fourier component of that variable ($[A] \equiv A_{m,n}$), superscripts denote iteration level, and subscripts indicate radial mesh position.

With this notation the components of the current (**J**) in finite difference form are

$$[J_\rho]^n_{i+1/2} = \frac{-m}{r_i}[B_\phi]^n_{i+1/2} + n[B_\theta]^n_{i+1/2},$$

$$[J_\theta]^n_i = n[B_\rho]^n_i - \frac{[B_\phi]^n_{i+1/2} - [B_\phi]^n_{i-1/2}}{\Delta\rho},$$

and

$$[J_\phi]^n_i = \frac{\rho_{i+1/2}[B_\theta]^n_{i+1/2} - \rho_{i-1/2}[B_\theta]^n_{i-1/2}}{\rho_i \Delta\rho} - \frac{m}{\rho_i}[B_\rho]^n_i,$$

where $\Delta\rho$ is the radial mesh step and the subscript $i+1/2$ denotes a point of the intermediate mesh halfway between ρ_i and ρ_{i+1} (many of the variables are stored on this mesh as explained in Section 3b).

In finite difference form, the components of the equilibrium equation [Eq. [6]] are

$$[F_\rho]^{n+1}_i = [B^\phi_i J^\theta_i]^n - [B^\theta_i J^\phi_i]^n - \frac{[P]^n_{i+1/2} - [P]^n_{i-1/2}}{\Delta\rho},$$

$$[F_\theta]^{n+1}_{i+1/2} = \frac{[B^\rho_i J^\phi_i]^n + [B^\rho_{i+1} J^\phi_{i+1}]^n}{2} - [B^\phi_{i+1/2} J^\rho_{i+1/2}]^n + \frac{m[P]^n_{i+1/2}}{\rho_i},$$

and

$$[F_\phi]^{n+1}_{i+1/2} = [B^\theta_{i+1/2} J^\rho_{i+1/2}]^n - \frac{[B^\rho_i J^\theta_i]^n + [B^\rho_{i+1} J^\theta_{i+1}]^n}{2} + n[P]^n_{i+1/2}.$$

In finite difference form the flux conservation equation [Eq. (8)] is

$$\frac{[B^\theta/D_v]^{n+1}_{i+1/2} - [B^\theta/D_v]^n_{i+1/2}}{\Delta t} = n[v^\theta_{i+1/2}(B^\phi/D_v)_{i+1/2} - v^\phi_{i+1/2}(B^\theta/D_v)_{i+1/2}]^n$$

$$- \frac{[V^\rho_{i+1}(B^\theta/D_v)_{i+1} - V^\theta_{i+1}(B^\rho/D_v)_{i+1} - V^\rho_i(B^\theta/D_v)_i + V^\theta_i(B^\rho/D_v)_i]^n}{\Delta\rho}$$

and

$$\frac{[B^\phi/D_v]^{n+1}_{i+1/2} - [B^\phi/D_v]^n_{i+1/2}}{\Delta t}$$

$$= \frac{-m}{\rho_{i+1/2}} [V^\theta_{i+1/2}(B^\phi/D_v)_{i+1/2} - V^\phi_{i+1/2}(B^\theta/D_v)_{i+1/2}]^n$$

$$+ \frac{\rho_{i+1}[V^\phi_{i+1}(B^\rho/D_v)_{i+1} - V^\rho_{i+1}(B^\phi/D_v)_{i+1}]^n - \rho_i[V^\phi_i(B^\rho/D_v)_i - V^\rho_i(B^\phi/D_v)_i]^n}{\rho_{i+1/2}\Delta\rho},$$

where Δt is the timestep. From $\nabla \cdot \mathbf{B} = 0$ an equation for (B^ρ/D_v) is given:

$$[B^\rho/D_v]^n_i = (\rho_{i+1}[B^\rho/D_v]^n_{i+1} - \Delta\rho m[B^\theta/D_v]^n_{i+1/2} - \Delta\rho\rho_{i+1/2} n[B^\phi/D_v]^n_{i+1/2})\,\rho_i^{-1}.$$

This equation, together with the wall boundary condition $[B^\rho/D_v] = 0$, is sufficient to iteratively determine (B_ρ/D_v). Finally, the pressure equation [Eq. (9)] becomes, in finite difference form,

$$\frac{[P]^{n+1}_{i+1/2} - [P]^n_{i+1/2}}{\Delta t} = -\left[V^\rho_{i+1/2}\frac{(P_{i+1} - P_i)}{\Delta\rho}\right]^n - \frac{1}{\rho_{i+1/2}}\left[V^\theta_{i+1/2}\frac{\partial P_{i+1/2}}{\partial\theta}\right]^n$$

$$-\left[V^\phi_{i+1/2}\frac{\partial P_{i+1/2}}{\partial\phi}\right]^n - \gamma[P_{i+1/2}(\nabla\cdot\mathbf{V})_{i+1/2}]^n,$$

where $\nabla \cdot \mathbf{V}$, in finite difference form, is

$$[\nabla\cdot\mathbf{V}]^n_{i+1/2} = \frac{1}{\rho_{i+1/2}}\left[(D_v)_{i+1/2}\Delta\rho^{-1}(\rho_{i+1}(V^\rho/D_v)_{i+1} - \rho_i(V^\rho/D_v)_i)\right]^n$$

$$+ \frac{1}{\rho_{i+1/2}}\left[(D_v)_{i+1/2}\frac{\partial}{\partial\theta}(V^\theta/D_v)_{i+1/2}\right]^n + \left[(D_v)_{i+1/2}\frac{\partial}{\partial\phi}(V^\phi/D_v)_{i+1/2}\right]^n.$$

Many of the above equations implicitly involve Fourier convolutions. For example, the last term of the last equation requires the convolution of V^ϕ and $1/D_v$.

ACKNOWLEDGMENTS

We acknowledge many useful discussions with members of the ATF group. In particular, the contributions of J. H. Harris and J. L. Cantrell to the heliac studies are gratefully acknowledged. We should also like to thank the Max-Planck Institut für Plasmaphysik and, in particular, Dr. R. Chodura and Dr. A. Schlüter, for providing us with a copy of their equilibrium code. Research was sponsored by the Office of Fusion Energy, U.S. Department of Energy, under Contract DE-AC05-840R21400 with Martin Marietta Energy Systems, Inc.

REFERENCES

1. J. M. GREENE AND J. L. JOHNSON, *Phys. Fluids* **4** (1961), 875.
2. D. LORTZ AND J. NÜHRENBERG, *Z. Naturforsch. A* **31**, 1277; *Nucl. Fusion* **17** (1977), 125.
3. R. CHODURA AND A. SCHLÜTER, *J. Comput. Phys.* **41** (1981), 68.
4. F. BAUER, O. BETANCOURT, AND P. GARABEDIAN, "A Computational Method in Plasma Physics," Springer-Verlag, New York, 1978.
5. J. F. LYON, B. A. CARRERAS, J. H. HARRIS, J. A. ROME, R. A. DORY, L. GARCIA, T. C. HENDER, S. P. HIRSHMAN, T. C. JERNIGAN, J. SHEFFIELD, L. A. CHARLTON, R. H. FOWLER, H. R. HICKS, J. A. HOLMES, V. E. LYNCH, B. F. MASDEN, D. L. GOODMAN, AND S. A. HOKIN, Oak Ridge National Laboratory Report ORLN/TM-8496, 1983.
6. A. H. BOOZER, T. K. CHU, R. L. DEWAR, H. P. FURTH, J. A. GOREE, J. L. JOHNSON, R. M. KULSRUD, D. A. MONTICELLO, G. KUO-PETRAVIC, G. V. SHEFFIELD, S. YOSHIKAWA, AND O. BETANCOURT, *in* "Plasma Physics and Controlled Nuclear Fusion Research," Vol. 3, p. 129, IAEA, Vienna, 1983.
7. A. H. BOOZER, *Phys. Fluids*, **25** (1982), 520.
8. G. KUO-PETRAVIC, A. H. BOOZER, J. A. ROME, AND R. H. FOWLER, *J. Comput. Phys.* **51** (1983), 261.
9. L. GARCIA, B. A. CARRERAS, J. H. HARRIS, H. R. HICKS, AND V. E. LYNCH, *Nucl. Fusion* **24** (1984), 115.
10. B. A. CARRERAS, H. R. HICKS, J. A. HOLMES, V. E. LYNCH, L. GARCIA, J. H. HARRIS, T. C. HENDER, AND B. F. MASDEN, *Phys. Fluids* **26** (1983), 3569.